

Neutron sensitive beam loss monitoring system for the European Spallation Source linac

I. Dolenc Kittelmann^{✉,*}, F. dos Santos Alves[✉], E. Bergman, C. Derrez, V. Grishin, K. Rosengren, and T. J. Shea
European Spallation Source ERIC, 224 84, Lund, Sweden

P. Legou, Y. Mariette[✉], V. Nadot[✉], T. Papaevangelou[✉], and L. Segui[✉]
IRFU-CEA, Université Paris-Saclay, F-91191, Gif-sur-Yvette, France

W. Cichalewski[✉], G. W. Jabłoński[✉], W. Jałmużna, and R. Kiełbik[✉]
Department of Microelectronics and Computer Science,
Łódź University of Technology, 93-005, Łódź, Poland

 (Received 3 December 2020; revised 17 November 2021; accepted 23 December 2021; published 25 February 2022)

The European Spallation Source (ESS), currently under construction in Lund, Sweden, will be a neutron source based on a partly superconducting linac. The ESS linac will be accelerating protons to 2 GeV with a peak current of 62.5 mA and ultimately delivering a 5 MW beam to a rotating tungsten target for neutron production. For a successful tuning and operation of a linac, a beam loss monitoring (BLM) system is required. BLM systems are designed to protect the machine from beam-induced damage and unnecessary activation of the components. This paper focuses on one of the BLM systems to be deployed at the ESS linac, namely the neutron sensitive BLM (nBLM). An overview of the ESS nBLM system design will be presented. In addition to this, results of the tests performed with the full nBLM data acquisition chain will be discussed. These tests represent the first evaluation of the system prototype in a realistic environment. They served as an input to initial study of the procedure for neutron detection algorithm configuration discussed in this contribution as well.

DOI: [10.1103/PhysRevAccelBeams.25.022802](https://doi.org/10.1103/PhysRevAccelBeams.25.022802)

I. INTRODUCTION

The European Spallation Source (ESS) will be a material science research facility, which is currently being built in Lund, Sweden. Once constructed, it will provide neutron beams for neutron-based research [1,2]. The neutron production will be based on bombardment of a rotating tungsten target with a proton beam of 5 MW average power and macropulse beam current of 62.5 mA. A linear accelerator (linac) will accelerate protons to 2 GeV and transport them toward the target through a sequence of normal-conducting (NC) and superconducting (SC) accelerating structures (Fig. 1). The NC linac consists of an ion source, low energy beam transport (LEBT), radio frequency quadrupole (RFQ), medium energy beam transport (MEBT), and drift tube linac (DTL) sections. On the other hand, Spoke, medium beta and high beta elliptical cavities together with high energy beta transfer (HEBT) line

comprise the SC linac. The ESS linac is operated at 352.21 MHz and 704.42 MHz frequency in the initial and end parts, respectively. During neutron production beam is delivered to the target in 2.86 ms long macropulses with a repetition rate of 14 Hz, corresponding to a duty cycle of 4%. Pulse length, repetition rate as well as macropulse beam current can during linac tuning and commissioning phases reach values as low as 5 μ s, 1 Hz and 6 mA, respectively.

As in the case of all future high-power accelerators, the ESS linac operation will be limited by beam losses if machine activation is to be kept low enough for hands-on maintenance. Moreover, loss of even a small fraction of intense ESS beam can result in a significant increase of irradiation levels, ultimately leading to damage of the linac components. Beam loss monitoring (BLM) systems are designed to provide information about beam loss levels. Thus, they play an important role in machine fine-tuning as well as machine protection from beam-induced damage by detecting unacceptably high beam losses and promptly inhibiting beam production.

Two types of BLM systems differing in detector technology have been conceived at ESS. The neutron sensitive BLM (nBLM) system is based on 82 neutron detectors primarily covering the lower energy part of the ESS linac.

*irena.dolenckittelmann@ess.eu

Published by the American Physical Society under the terms of the *Creative Commons Attribution 4.0 International license*. Further distribution of this work must maintain attribution to the author(s) and the published article's title, journal citation, and DOI.

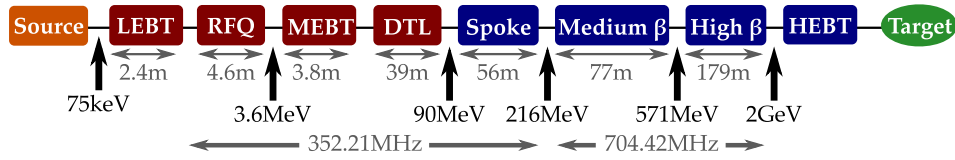


FIG. 1. A block diagram of the ESS linac [1,2]. The normal-conducting (NC) linac is composed of an ion source, radio frequency quadrupole (RFQ), drift tube linac (DTL), low (LEBT) and medium energy beam transport (MEBT) sections. Spoke resonators, medium beta and high beta elliptical cavities together with high energy beta transfer (HEBT) line constitute the superconducting (SC) linac. Red and blue color refer to NC and SC parts of the linac, respectively.

Conversely, the ionization chamber-based BLM (ICBLM) system consists of 266 ionization chambers located almost exclusively throughout the SC parts of the linac [3].

This contribution aims to report an overview of the ESS nBLM system design. In addition to this, results of the tests performed with the first prototype in realistic environment are presented together with the initial analysis of the procedure to configure the neutron detection algorithm.

II. DETECTOR DESIGN

The ESS nBLM system is based on neutron-sensitive Micromegas devices [4], specially designed to primarily cover the lower energy part of the ESS linac. Monte Carlo simulation studies were used to optimize the detector design and locations in order to assure coverage and redundancy for the machine protection purposes and provide information on beam loss location for the diagnostic purposes [5–7].

One of the challenges when measuring beam losses in a linac is related to the rf-induced background. This background is mainly due to the electron field emission from rf cavity walls resulting in bremsstrahlung photons created on the cavity or beam pipe materials [8]. For this reason, the nBLM detectors are designed to be sensitive to fast neutrons and exhibit low sensitivity to low-energy photons.

Additionally, the signals due to thermal neutrons are suppressed as they may not be directly correlated to the beam losses. This is achieved by equipping the detector with suitable absorber and neutron converter materials.

Two types of nBLM detectors with complementary functionality have been developed. Fast detectors (nBLM-F) are designed to detect fast losses when high particle fluxes due to accidental beam losses are expected. On the other hand, slow detectors (nBLM-S) primarily aim to monitor slow losses when low particle fluxes are expected. Details of the final detector module design and performance are available in [9–12].

Signal pulses from both detector types, nBLM-F and nBLM-S, exhibit the same time characteristics, however neutron moderation in case of nBLM-S delays a larger fraction of events by an amount of time ranging from tens of ns to $\sim 200 \mu\text{s}$. A typical signal produced by an incoming particle in these detectors is a negative pulse with a rise time of 30–50 ns and pulse duration of 100–200 ns, depending on the applied electric fields in the detector chamber.

III. COVERAGE AND DETECTOR LAYOUT

Following the goal of nBLM system as the primary loss monitor in the NC parts of the ESS linac, the majority of detectors will be placed in the DTL section (Fig. 1). Here

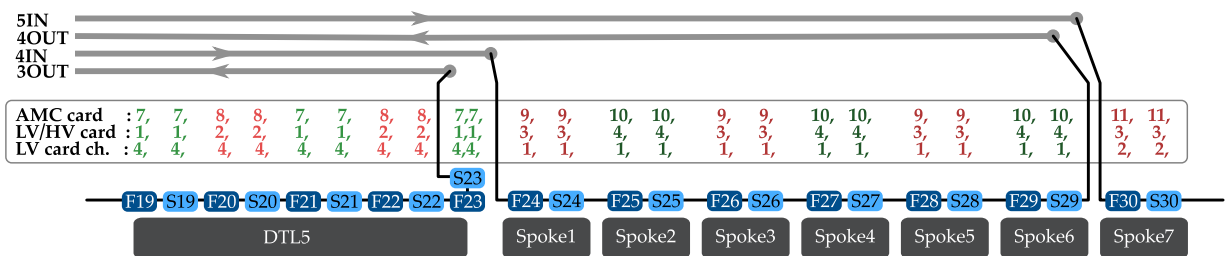


FIG. 2. Detector and cabling layout for DTL tank 5 and initial 7 subsections of the Spoke section. Each Spoke subsection consists of two parts, a so called linac warm unit (LWU) with a pair of quadrupole magnets and a cryomodule housing two spoke cavities. Light and dark blue squares, respectively, indicate nBLM-S and nBLM-F detector locations along these linac sections. Which AMC, HV and LV card number as well as LV card channel each detector connects to is represented with green or red numbers stated above the detector. Here green and red color respectively mark odd and even detector group type. For example, detectors F19, S19, F21, S21, S23, and F23 belong to one of the odd groups and connect to AMC card 7, HV card 1 and the fourth channel on LV card 1. Similarly, detectors F20, S20, F22, and S22 belong to one of the even groups and connect to AMC card 8, HV card 2, and fourth channel on LV card 2. Shade of green and red color indicates different BEE racks, namely AMC cards 9 and 11 sit in the same rack, while card 8 is located in a different rack. Gas loops for circulating the gas through a series of detectors are indicated with grey and black lines representing the long haul and flexible tubes, respectively. Here “IN” refers to a distribution and “OUT” to a return long haul gas pipe. For example, the fourth gas loop circulates the gas through detectors in the first 6 Spoke subsections.

detectors will be positioned at every $\sim 1/4$ of a DTL tank length (~ 1 m), resulting in 8 detectors per each of the five DTL tanks and a pair at the end of the DTL section. This placement selection was determined through Monte Carlo simulation campaign of lost protons for a set of localized beam loss scenarios differing in beam parameters and locations along the DTL section. The resulting standard deviation of the secondary neutron distributions ~ 20 cm away from the tanks was found to vary between 0.9–3.6 m [6] depending on the loss scenario. The simulations were performed with the use of Geant4-based [13–15] simulation and coding framework [16,17] developed by the ESS neutron detector group. Details about the simulation setup and implemented ESS linac geometry can be found in [5,6].

A significant number of detectors will be located in the Spoke section following the DTL for smooth transition in coverage between NC and SC parts of the linac with nBLM as the primary monitor in the former parts and ICBLM in the latter parts of the linac. The arrangement also allows an option to compare the measurements between the two systems and potentially better understand the background signal. Other high-energy parts of the linac are only sparsely populated with nBLM detectors.

The majority of the nBLM detectors will alternate between the nBLM-F and -S types in the DTL and along the Spoke region (Fig. 2). In Spoke section one slow detector will be located at each cryomodule. One fast detector will be placed at each Spoke linac warm unit (LWU), a region with a pair of quadrupole magnets. One of each detector type will be placed together at selected locations, namely at the end of DTL, two locations in MEBT and at few locations in SC sections after the Spoke section.

IV. SYSTEM ARCHITECTURE

A schematic overview of the nBLM system architecture is shown in Fig. 3. Each detector is enclosed in a detector module together with custom front-end electronics (FEE) [11,12]. Analog signals are routed from detector modules in the linac tunnel to the back-end electronics (BEE) housed in racks located in the Klystron Gallery building at the ground level. Here, the signal is first digitized and sampled at 250 MS/s rate by a dc-coupled, 8-channel, 16-bit ADC (IOxOS ADC3111 FMC [18]). The signal is then processed in real time by a MTCA.4-based AMC board (IOxOS IFC1410 [19]) equipped with Xilinx Kintex Ultrascale FPGA. The board handles up to 6 detector channels simultaneously. It additionally manages communication to the machine protection system (MPS [20]) and issues a request to inhibit beam production if unacceptably high beam losses are measured (see Sec. V for further details). The data acquisition is synchronized with the ESS Timing system [21] through an interface card (EVR) located in each BEE crate.

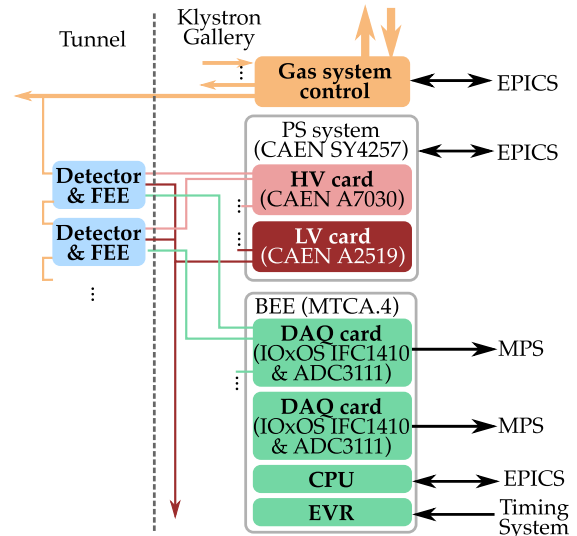


FIG. 3. Schematic view of the nBLM system architecture consisting of detector modules (detectors with front-end electronics—FEE), back-end electronics (BEE) for data acquisition (DAQ), gas system, power supply (PS) system providing high (HV) and low (LV) voltage to detector modules and EPICS-based [22] control system. The system connects to the ESS machine protection (MPS [20]) and ESS timing [21] systems.

Two CAEN SY4527 [23] crates will be used to control high (HV) and low (LV) voltage power supplies. The 48-channel module CAEN A7030 [24] will bias the detectors, while the 8-channel CAEN A2519 [25] will power the FEE, where one LV channel is used per group of up to 6 detectors.

The nBLM detectors, or Micromegas detectors, are gaseous particle detectors that require a continuous gas flow of 1–2 L/h to insure a stable operation on a timescale of years. The gas mixture planned to be used consists of He and 10% CO₂. However, replacing CO₂ with a different quencher like ethane offers higher gain and thus improves detector operational stability, though at the cost of longer signal pulses. As follows from section V, shorter signal pulses are preferred in order to retain the power of neutron/ γ discrimination on event-by-event basis for higher neutron fluxes. The choice of using ethane instead of CO₂ is currently under investigation.

The premixed gas is distributed to the detectors from gas bottles located in a shelter outside the Klystron Gallery building. One distribution and one return stainless steel gas pipe is routed from the bottles to a dedicated rack inside the building. The rack houses custom crates for PLC-based control and monitoring of the gas flow and pressure. Here, both distribution and return lines are split in 6 long stainless steel pipes which are further routed to the accelerator tunnel. The 12 pipes end at different points along the linac where they are continued with polyurethane flexible tubes to form 6 loops. Each of these loops circulates gas through a group of 10–20 neighboring detectors connected with

polyurethane tubes in series. The loops are indicated in Fig. 2 with grey and black lines representing long (stainless steel) and short (polyurethane) gas tubes, respectively.

Monitoring and control of the system is managed through an EPICS-based [22] software. The software for data acquisition runs on the CPUs located in the MTCA crates. As for the gas and CAEN power supply system, the EPICS software runs on a virtual machine cluster and internal CAEN CPU, respectively.

The detectors are organized in three types of groups, namely odd, even and mixed groups. The groups are formed based on the cabling layout of the read-out electronics and detector powering connections. This arrangement has been adopted in order to increase the system robustness and to avoid situations when a certain electronic failure results in system not being able to react on dangerous beam conditions for larger part of the linac. Linac parts up to and including Spoke section that contain majority of the nBLM detectors, are covered by the odd and even groups. These are formed by collecting odd and even pairs of neighboring fast and slow detectors. Each of these groups has its detectors connected to a different BEE rack. The mixed group type covers the rest of the detectors sparsely located in the high-energy parts of the linac. In this case, the detectors are grouped in such a way that the connection to the BEE is routed to the closest rack. The longest signal cable length of this layout is estimated to be below 100 m.

Both HV and LV connections follow the same detector grouping as the signal connections. However, due to a limited number of HV and LV crates, complete separation between connections for odd and even groups down to the rack level is not possible. Instead, each odd or even group of detectors connects to a dedicated LV and a dedicated HV card, both located in the first out of two available power supply crates. Similarly, each mixed group has its detector modules biased by a dedicated HV and LV card, both located in the second power supply crate for nearly all mixed groups, while the rest of the mixed groups have their LV and HV cards housed in the first crate. In order to avoid unnecessary grounding issues, attention is also paid to ensure that a set of detectors connected to a certain AMC card has their FEE powered by a dedicated LV channel.

The idea of HV, LV and signal connections is schematically presented in Fig. 2 for part of the linac.

V. DATA PROCESSING

Monte Carlo-based simulation studies of lost protons for a set of loss scenarios along the DTL part of the ESS linac [5,6] were performed. The results further served as an input to Monte Carlo simulations [7] of detector response. These show that at higher loss levels, the nBLM system can experience pileup of neutron events and eventually transition from single event counting to current mode of operation. The transition is performed

automatically by the FPGA-based real-time data processing as described below.

The main task of a BLM system is to detect beam instabilities that might cause damage to the linac equipment. The system is designed to inhibit the beam production when potentially harmful beam conditions due to fast losses are detected. When such conditions are detected, the system triggers a request to machine protection system (MPS) to stop the beam production by changing the BEAM_PERMIT signal from the “OK” to the state “NOT OK.” This signal is a binary signal continuously transmitted to the MPS which further handles beam production inhibition whenever a sensor system like BLM sends a request. In addition to machine protection against fast losses, the BLM system provides diagnostic information about the beam loss levels. This information is valuable for machine tuning and operation in order to avoid unnecessary activation of the linac equipment.

This is achieved by continuous processing of digitized raw signal from each nBLM detector in order to provide the neutron count, N_n , for each detector separately. For a given detector, the value N_n is extracted as the number of neutrons observed in a monitoring time window (MTW) and relates to the beam loss around and upstream of the detector location. The duration of MTW was selected to be 1 μ s in order to comply with both the 5 μ s response time requirement of the system for machine protection purposes and with time characteristics of the signal pulse produced by an incoming single neutron.

A schematic overview of the key steps in the data processing chain for one nBLM detector is given in Fig. 4. At the beginning of the chain, a fixed detector-dependent pedestal value is subtracted from each raw data sample. The processing is continued with the neutron detection algorithm (NDA), primarily providing N_n every μ s.

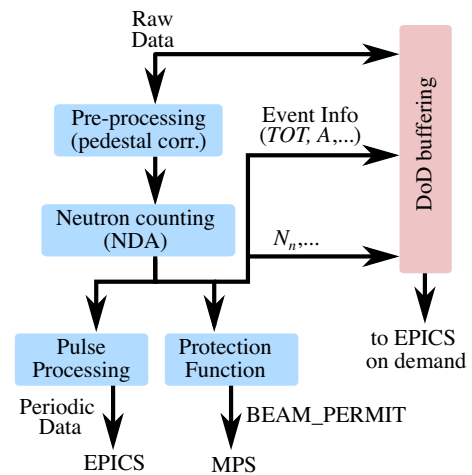


FIG. 4. Simplified block diagram of the data processing chain for one nBLM detector. DoD refers to the data that can only be retrieved on demand, for explanation see text at the end of Sec. V.

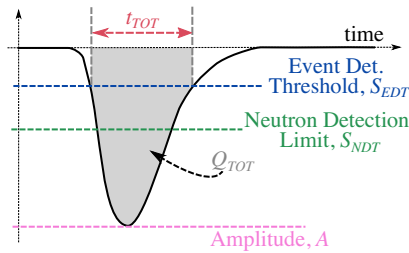


FIG. 5. Sketch of a neutron event with NDA settings and some of the pulse characteristics.

The NDA starts by first identifying interesting events (IEs). An IE is considered to start whenever the (negative-going) signal crosses a certain event detection threshold (S_{EDT}) and to end when signal raises back above this value (Fig. 5). For each IE certain pulse characteristics (amplitude A , time-over-threshold t_{TOT} , event charge Q_{TOT} , etc.) are extracted and stored in a so called `EventInfo` structure.

An IE can be classified as a neutron or non-neutron event. Furthermore, a neutron event can either be due to a single neutron or several neutrons. The latter occurs when the rate of incoming neutrons is too high for the system to distinguish between two single neutron events, which leads to event pileup. Non-neutron events are caused by noise spikes or background particles (mostly x- and γ -rays) with their rate depending on environment and above-mentioned S_{EDT} for a given set of detector operation conditions.

The basic idea behind the NDA is to distinguish between single neutron (SN), pileup (PU), and non-neutron (NN) events and accordingly extract N_n every MTW. The number of neutrons is estimated through either single neutron counting (SNC) or charge (Q-) method. In case of a SN event, N_n is increased by one (SNC method). The Q-method is used for a PU event, where N_n is estimated from the total event charge, Q_{TOT} , extracted as the integral of the signal over the event t_{TOT} (see Fig. 5). The number of neutrons is then determined as $N_n = \frac{Q_{TOT}}{\langle Q_{TOT} \rangle}$, where $\langle Q_{TOT} \rangle$ in general represents the average value of Q_{TOT} for SN event.

An IE is regarded as a SN event when its t_{TOT} exceeds a certain limit ($t_{TOT,SNT}$) and amplitude A (a negative number) falls below a predefined neutron detection threshold (S_{NDT}). In case the t_{TOT} of a neutron event is large enough (larger than $t_{TOT,PUT}$) the event is recognized as a PU. An IE which does not qualify as a neutron event is considered as a NN event.

The above description presents a simplified view of the NDA. To improve noise immunity, hysteresis in S_{EDT} is introduced in the IE identification. Furthermore, the need to report the neutron counts per unit of time without unnecessary delays complicates the data processing, as one cannot wait indefinitely for a long event to end. Therefore, certain IEs are terminated at the MTW edge and need special care. There are two types of IEs that end

on MTW edge. The first type are those that fulfilled the single neutron conditions before reaching or at the MTW edge but did not end before that. In this case the neutron count of both current and subsequent IE is extracted with the Q-method. The second type of IEs, that end on an MTW edge, are NN events with t_{TOT} larger than a predefined value, which was selected to be equal to $t_{TOT,PUT}$.

The N_n values are streamed at 1 MHz to the input of protection function algorithm, which is continuously assessing if conditions to inhibit beam production have been met. Here the data is first passed through configurable filters and then compared to the channel-dependent thresholds. The final result is a `BEAM_PERMIT` signal that is aggregated over all functioning channels on each AMC, and is continuously transmitted to the MPS.

The N_n values together with other NDA outputs are additionally used to compute several statistics called periodic data. These are typically extracted on every machine cycle (14 Hz) for monitoring purposes. An example of such monitoring variable is N_n averaged over full machine cycle. In addition to the periodic data, certain types of data originating from various stages of processing are being buffered and can be retrieved on demand (data on demand—DoD). This among other includes raw detector signal (sampled at 250 MHz), `EventInfo` structure (for each IE) and neutron counts N_n (arriving at 1 MHz rate).

As both slow and fast detector exhibit the same time characteristics of the signal, the same algorithm is used in both cases. Details about the firmware implementation can be found in [26].

VI. FIRST PROTOTYPE TEST

In summer 2018, an nBLM-F pre-series detector module was installed at LINAC4 [27,28] at CERN in order to perform nBLM prototype tests under conditions close to the ones expected in the ESS DTL section. The module was placed close to the beam pipe at the intertank region between DTL tank 1 and 2, where H^- beam energy reaches ~ 12 MeV.

LINAC4 is the first accelerator in the LHC injection chain. It has transitioned from commissioning phase to operation in 2020. It operates at the frequency of 352.21 MHz and delivers H^- beam with a nominal energy of 160 MeV and maximum beam pulse of 600 μs to the Proton Synchrotron Booster (PSB), the next stage of the LHC injection chain. The beam macro pulse length and structure are tailored with a prechopper and chopping system located in LEBT and MEBT sections, respectively. The prechopper removes the head and tail of the macro beam pulse coming from the ion source. The MEBT chopper is further used to create sharp edges at the beginning and end of the macro pulse. Additionally, it can remove selected micro-bunches in the 352 MHz sequence inside the pulse to match the beam to the PSB distribution system. The nominal average current along the

resulting beam pulse is 25 mA. The linac can pulse at maximum repetition rate of 2 Hz.

Two nBLM data-taking campaigns were carried out during LINAC4 commissioning runs in 2018 and 2019. In this section the first campaign is discussed. The campaign took place in December 2018 and represents the first evaluation of the full nBLM DAQ chain including a detector in realistic environment. The data was additionally acquired with an oscilloscope during separate dedicated time periods in order to focus on assessment of the detector performance. The results of the data collected with the nBLM DAQ are reported in this paper, while conclusions from the data recorded with an oscilloscope are discussed in [9,10]. Note, that during both 2018 and 2019 test campaign, the linac was operated at 1.2 s beam pulse spacing corresponding to repetition rate of 0.83 Hz.

The nBLM DAQ prototype under test was at an early stage of its development with a running NDA and possibility to manually trigger data on demand, including raw unprocessed data stream in a time window of up to 2 s. The prototype did not include the periodic data monitoring and protection algorithm features, however, the main processing chain was in its final version.

The aforementioned `EventInfo` data for each IE were collected in several acquisition runs with duration ranging from 5 min to 8 h. Figure 6 shows distribution of number of IEs over amplitude, extracted through an offline analysis from all `EventInfo` focused data acquisition runs. Due to the need of splitting certain pulses in the real-time processing, offline analysis includes reconstruction of recorded events in order to extract the real pulse characteristics like amplitude. This results in differences between reconstructed and raw event amplitude distributions as demonstrated in Fig. 6. The reconstructed distribution exhibits expected shape with the first slope due to the noise and second slope due to the γ particles primarily induced by the rf. Neutrons are observed to dominate at amplitudes above ~ 30 mV as demonstrated in Fig. 6.

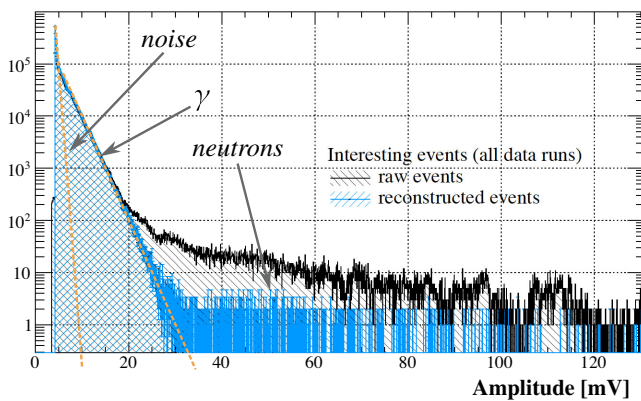


FIG. 6. Distribution of number of IEs over amplitude collected at LINAC4 in 2018. Blue histogram represents reconstructed data, while black refers to the data as recorded.

The results are consistent with the results obtained from the oscilloscope data [9,10]. Note, that each merged reconstructed event is formed from at least two raw events. Hence, the number of events in the reconstructed histogram can be less or equal to the number of events in the raw event histograms.

The γ related part of the distribution follows the exponential shape due to Compton scattering as the dominant γ process, which transforms the incoming γ -rays to recoil electrons further producing measurable electronic signal [10,12]. As the nBLM-F type was used in these tests, the recorded amplitude distribution follows a continuous spectrum overlapping with the γ part. The measured amplitude spectrum depends on the spectrum of the incoming neutrons as well as the continuous energy spectrum of the recoil protons produced by the neutrons in the convertor material. Note, that in case of the nBLM-S type, clearer separation between γ and neutron contribution is observed due to the difference in dominant process for neutron detection [10].

Distributions of reconstructed IEs over amplitude and time inside the machine cycle period of the LINAC4 (1.2 s) have been extracted for each data run separately (Fig. 7). The obtained distributions may be used to reveal the rf and beam pulse average structure, assuming that neutrons and γ particles signify the presence of beam and rf pulse, respectively. Here, the neutrons are expected to dominate at higher amplitudes while the γ particles may be observed at intermediate amplitudes between noise and neutron dominated regions as indicated in Fig. 7.

The prototype at this stage did not include synchronization with the LINAC4 timing system. As a result, the observed rf and beam pulse duration are larger than expected with longer data runs exhibiting larger increase. The effect is attributed to the ADC clock drift. In order to correct for this effect in the offline analysis, a constant clock drift was assumed and a scan over ADC sampling

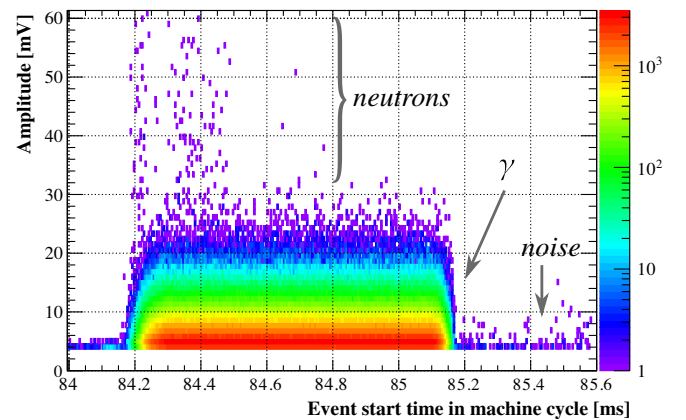


FIG. 7. Distribution of reconstructed IEs over amplitude and time inside the LINAC4 machine cycle period for an 8-hour long data run.

period was performed for each run separately. The best approximation for the ADC sampling period was extracted as the one giving the sharpest rf pulse edges. Typical value for the optimal clock period was found to be around a factor of 5.6×10^{-6} (5.6 ppm) larger than the nominal 4 ns. This results in rf pulse FWHM (full width at half maximum) length and 90% length of $\sim 880 \mu\text{s}$ and $\sim 840 \mu\text{s}$, respectively. The beam pulse length was estimated to be roughly $\sim 150 \mu\text{s}$, though partial presence in the first $\sim 100 \mu\text{s}$ can be observed. These pre-beam pulse neutrons are discussed in Sec. VII.

The extracted pulse lengths and shapes for both rf and beam are in agreement with the results obtained from the oscilloscope data [9,10]. The results are also consistent with the information received from LINAC4 operation and commissioning team. The LINAC4 rf and beam pulse length were communicated to be stable at $\sim 880 \mu\text{s}$ and $150 \mu\text{s}$, respectively, throughout the period of the 2018 nBLM data taking. The exception is ~ 1 h when pulse length was set to $600 \mu\text{s}$, which may explain a few additional neutron hits in the range of ~ 84.5 – 84.8 ms visible in Fig. 7.

VII. BEAM LOSS DETECTION AND NDA CONFIGURATION

The focus of this section is the second data-taking campaign, which was carried out during LINAC4 commissioning in November and December 2019. A dedicated experiment was performed, where controlled beam losses were produced by the LINAC4 operation and commissioning team in order to study the nBLM detector and DAQ performance. The losses were generated by horizontal defocusing of the last quadrupole magnet in the LINAC4 MEBT line. The magnet is located ~ 4.4 m upstream from the nBLM detector, just before the DTL section. Different beam configurations were produced with two different loss levels, namely 4 mA and 10 mA, and beam pulse duration varying between $50 \mu\text{s}$, $100 \mu\text{s}$ and $200 \mu\text{s}$. The loss levels were estimated as the difference in signals from a Beam Current Transformer (BCT) located at ~ 4.5 m downstream and a BCT at ~ 14.5 m upstream of the nBLM detector. The former is situated at the end of the MEBT line while the latter at the end of DTL tank 3.

Two configurations of detector voltage settings have been used during this test campaign. The configuration used during the controlled loss period was the same as during December 2018. Here, the detector mesh and drift cathodes were biased with $V_{\text{mesh}} = 550$ V and $V_{\text{drift}} = 1500$ V, respectively. Later the detector voltages were lowered to $V_{\text{mesh}} = 525$ V and $V_{\text{drift}} = 1475$ V in order to limit beam induced discharging in the detector. Original higher voltage settings were selected for clearer separation of gamma background events from the noise. Both configurations exceed the ESS operation point, which is foreseen to be $V_{\text{mesh}} = 500$ V and $V_{\text{drift}} = 750$ V [9,10].

The primary aim of this data run was to verify the results from 2018 campaign with the advanced version of the nBLM DAQ prototype. Among other improvements, this prototype allowed synchronization with the LINAC4 timing system. The synchronization was performed through LINAC4 machine cycle start trigger signals, which were used to capture cycle start timestamps. These timestamps further served for timestamp interpolation of the ADC time steps between the cycles, which is applied on the software level during the extraction of Data on Demand. In addition to this, the prototype offered Periodic Data monitoring features on the firmware level, though the focus during this campaign was again collecting the DoD, mostly from the EventInfo data stream. As in the case of 2018 results, reconstruction of the recorded EventInfo data through offline analysis was required in order to extract real pulse characteristics. A typical time evolution during the rf pulse together with an example of γ signal recorded in the raw data stream are given in Fig. 8.

Figure 9 shows distribution of reconstructed IEs over amplitude and start time in LINAC4 cycle for events

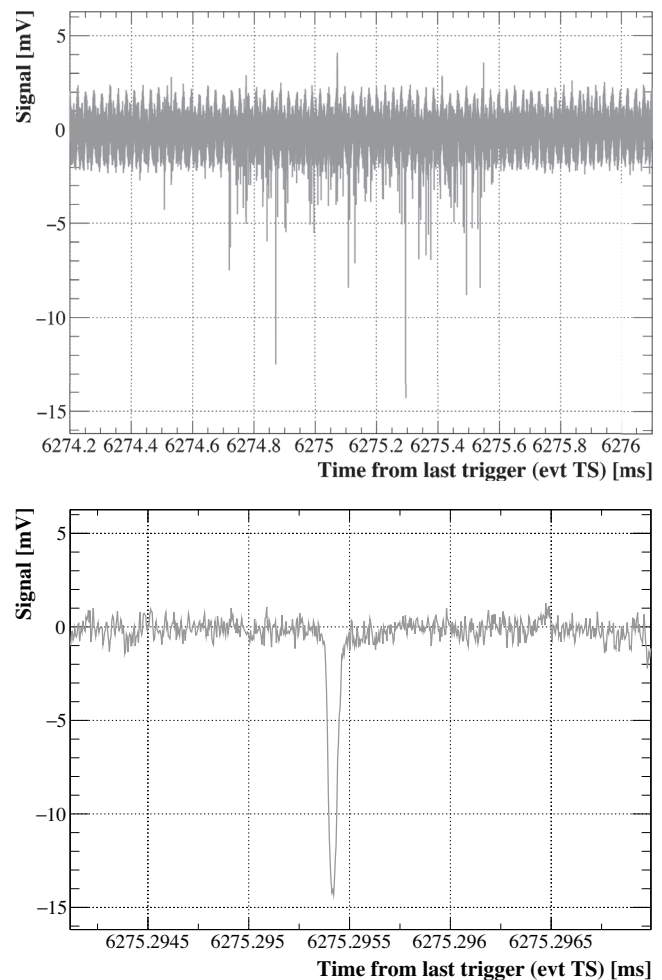


FIG. 8. Example of signals recorded in raw data during rf pulse (top) and a magnified view of one of the γ signals (bottom).

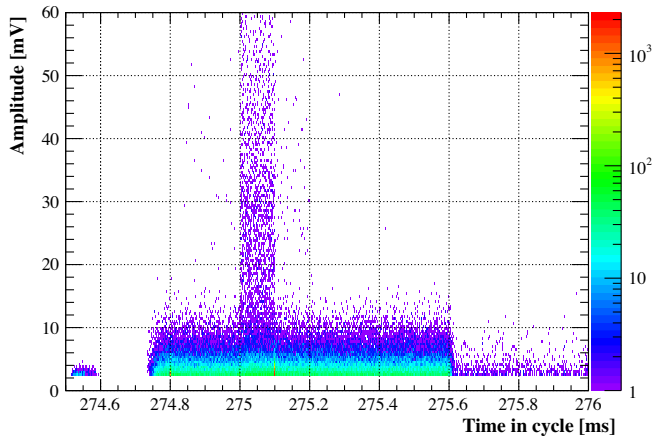


FIG. 9. Distribution of reconstructed IEs over amplitude and time in LINAC4 machine cycle period for data collected during the controlled loss experiment in 2019 data-taking campaign.

collected during the entire controlled loss experiment lasting over 30 min. The figure displays distinctive separation of neutron, γ and noise regions. Beam and rf pulse time structures can be readily estimated from the distributions of reconstructed IEs over the time in cycle. The results for the case of the data collected during the controlled loss period are given in Fig. 10. These histograms were extracted from Fig. 9 by projecting the events with amplitude above the cut-off threshold on the horizontal axis. The average beam pulse may be observed with an appropriate choice of higher amplitude cut-off threshold resulting in selecting only neutrons, while the average rf pulse structure is revealed in histograms with no or low amplitude cut. Figures 9 and 10 demonstrate 200 μ s and 100 μ s long beam pulses starting at 275 ms as indicated by event amplitudes above ~ 15 mV. As the produced beam pulse was set to 100 μ s for most of the controlled loss time period, the distributions exhibit larger fraction of events inside the first 100 μ s of the beam pulse. The results for beam pulse duration and start inside the cycle are in agreement with the information received from the LINAC4 operation team as well as the result extracted from the data collected with the oscilloscope [10].

As in the case of 2018 results, a small fraction of neutrons is observed in the ~ 274.8 – 275 ms time window prior to the beam pulse. This time window matches with the MEBT chopper time window for removing the head of the beam macropulse. The number of pre-beam pulse neutron events was observed to vary from few 10^{-3} counts/cycle to $\sim 4 \times 10^{-2}$ counts/cycle depending on the LINAC4 commissioning activity. Due to their time window of occurrence inside the machine cycle they may be explained by mismatching of the beam properties leading to not fully chopped beam pulse.

The nBLM results in Figs. 9 and 10 indicate an rf pulse duration of ~ 870 μ s. This value fits with the results extracted from the oscilloscope data, though it slightly

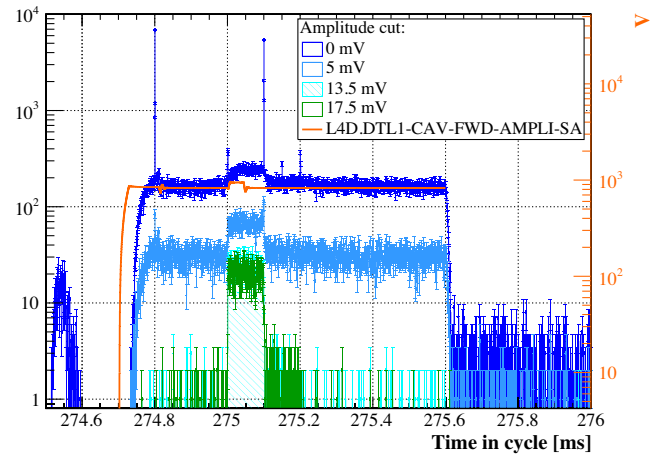


FIG. 10. Projections of the histogram from Fig. 9 on the time axis for different threshold cuts on the minimum event amplitude. Orange scale on the right side of the plot refers to the scale for the measurement marked with orange line. This line represents the cavity forward rf amplitude of the DTL tank 1 as measured by the LINAC4 operations team.

differs from the expected 900 μ s. The cavity forward rf amplitude of the DTL tank 1 as measured by the LINAC4 operation team is also shown in Fig. 10 for comparison. The difference in the initial part of the rf pulse can be explained by the cut on the amplitude (S_{EDT}) in the data processing chain. This cut results in a delayed start of the measured nBLM amplitude distribution compared to the cavity forward amplitude as observed in Fig. 10. Note, that forward amplitude measurement was performed on a different day than controlled loss experiment took place, however with the same rf configuration.

Figures 9 and 10 show increased rates of IEs with amplitude in the noise region at certain times inside the cycle, for example at 274.8 ms or 275 ms. These are believed to be due to the disturbances coming from the MEBT chopper. The assumption is based on the beam pulse durations during this experiment and information received from the LINAC4 commissioning team. Noise events, appearing outside the rf pulse in the time window 274.5–274.6 ms, are suspected to be due to the baseline fluctuations or noise pick-up related to either the ion source or LEPT chopper operation causing interference or disturbances in the power grid. Further tests in LINAC4 noise environment would reveal the actual cause. As noise environment is specific to each machine, it is planned to be investigated in more details at ESS linac as part of the nBLM system commissioning. Note, that pick-up noise or structures appearing on the baseline due to ON/OFF switching of different accelerator components do not interfere with neutron rate measurements as they can be easily discarded on the firmware level with the appropriate choice of neutron detection (S_{NDT}) or even event detection (S_{EDT}) threshold.

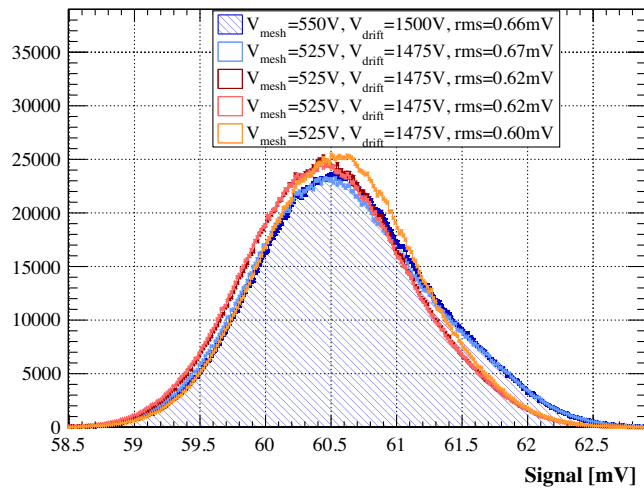


FIG. 11. Noise distributions extracted from raw data stream collected at different times and with the two voltage configurations used during the 2019 data-taking campaign. Noise RMS values are indicated in the legend.

As the detector was operated at increased voltage settings, a few beam-induced discharges in the detector were observed producing signals extending over few ms to ~ 10 ms. Due to the partly ringing-like signal shape of these discharges several fake IEs are identified even after the event reconstruction in the offline analysis. This results in increased noise levels after the rf pulse as observed in Figs. 9 and 10. Part of these events as well as the events resulting from the initial part of the discharge signals have been excluded by applying an upper limit on event t_{TOT} in the offline analysis.

The data from 2019 campaign was additionally used to estimate neutron rates and explore the role of `EventInfo` data stream in procedure for configuring the NDA settings. Acquiring `EventInfo` as well as neutron count data streams requires prior selection of appropriate event detection thresholds and pedestal. Both can be determined from noise distributions shown in Fig. 11. These noise distributions are extracted from raw data stream by sampling the data outside the beam and rf pulse windows. The pedestal value is identified as the mean of the measured noise distribution, while the RMS of this distribution is typically referred to as the measured noise. The event detection threshold is typically set to $\gtrsim 3$ times of noise RMS.

One of the essential parameters in single neutron identification is S_{NDT} , which can be extracted from IE amplitude distributions. Figure 12 shows amplitude distributions collected during the controlled loss time period and a ~ 7 h long overnight acquisition, when no beam was present. The detector voltage configuration was the same in both cases with values as given in the legend. The distribution of events with start time inside the rf pulse window as well as distribution without any cut on start time are presented in Fig. 12 for both data run periods. In case of

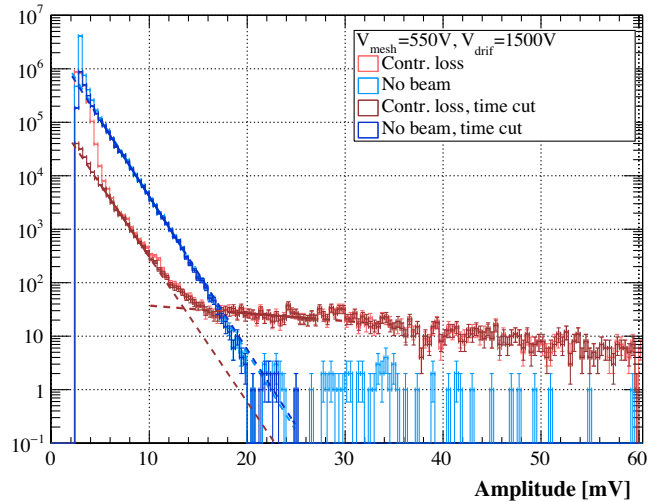


FIG. 12. Amplitude distributions extracted during the controlled loss experiment (red) and during an overnight data acquisition where beam was not present (blue). Dark and light colors refer to distributions extracted with and without cut on event start time applied, respectively. The dashed lines in the γ part indicate result of fitting an exponential shape to this region, with solid line marking range of the fit. The red dashed line in the neutron region is drawn to guide the eye.

the controlled loss run, increased noise levels in the region below ~ 5 mV are observed in the distribution without the time cut compared to the one where the cut was applied. This is to a larger extent attributed to discharge related events just after the rf pulse window.

Figure 12 indicates that neutrons dominate at amplitudes above ~ 15 mV. In addition to the detector voltage configuration this value depends on neutron and γ rates as well as energy spectrum, which all vary with the location along the linac. Note, that γ rates and energy spectrum further depend on the cavity accelerating field amplitude, though no noticeable change in the observed amplitude distribution in the γ part was observed during the 2019 campaign.

In order to make the selection of S_{NDT} value for given detector and its voltage settings independent of neutron rates, the value was determined as the amplitude, where γ rates become comparable to the background rate due to the cosmic neutrons. As the γ amplitude distribution follows an exponential shape, its contribution was extracted by fitting an exponential function to the amplitude distributions in the γ part. As indicated in Fig. 12 the values of parameter in the exponent for both controlled loss and no beam data period were found to be in agreement. Figure 13 shows normalized versions of two distributions from Fig. 12, namely controlled loss run (with start time cut applied) and overnight run (not time cut). The normalization factors were selected to give counts per second. For comparison, Fig. 13 additionally shows the curve representing γ background estimation as well as the distribution extracted from controlled loss run which has been corrected for the γ part.

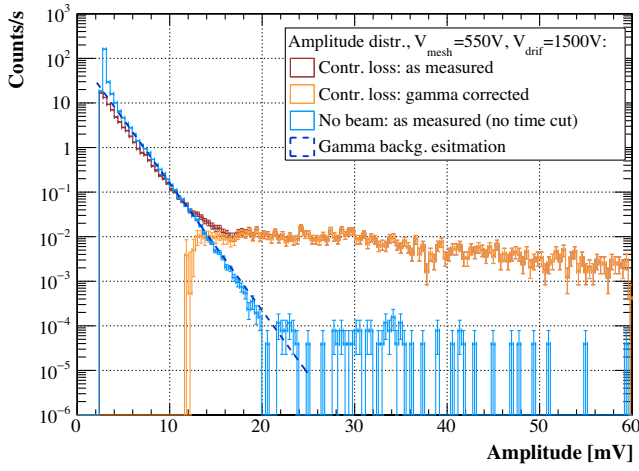


FIG. 13. Amplitude distributions extracted during the controlled loss experiment (red) and during an overnight data acquisition where beam was not present (blue). The distributions are normalized to give counts/s in each amplitude bin. Dark blue dashed line indicates estimated contribution of the γ part. Orange histogram represents the red distribution with γ correction applied.

In order to extract S_{NDT} as the amplitude where neutron background becomes comparable with the γ background part, relative efficiencies were extracted as a function of threshold amplitude (Fig. 14) for the two above-mentioned uncorrected distributions in Fig. 13. For a given threshold, the efficiency value was extracted by summing the count rates over all amplitude bins above the threshold. The value for S_{NDT} was found to be 17.6 mV. It was extracted from no-beam data as the intersection point of the exponential function fitted to the initial γ part (dashed dark blue line) with the one fitted to the initial neutron part of the

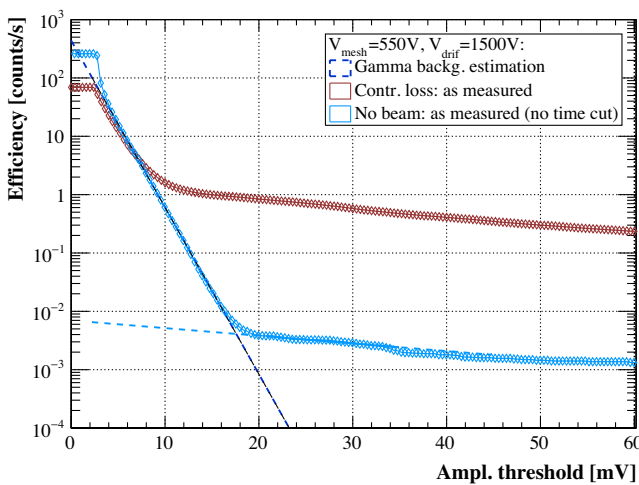


FIG. 14. Relative efficiency extracted from controlled loss (red) and no beam data (blue). Dashed lines indicate exponential functions fitted to the data in order to extract intersection point as the S_{NDT} value.

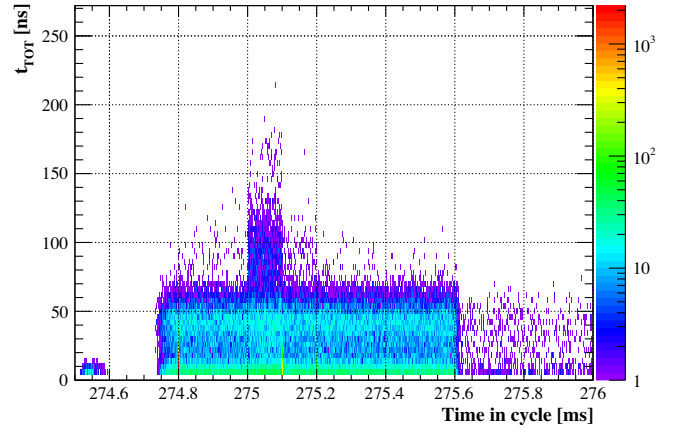


FIG. 15. Distribution of IE t_{TOT} over event start time inside machine cycle for data collected during the controlled loss experiment.

efficiency curve (dashed light blue line). Note, that the efficiency curves in Fig. 14 exhibit a flat initial part for thresholds below ~ 2 mV. This is due to the event detection threshold, S_{EDT} , applied on the firmware level in NDA. It results in events with amplitudes lower than this threshold (~ 2 mV in this case) not being recorded.

An additional NDA parameter required in single neutron identification is the lower limit on t_{TOT} of an interesting event ($t_{\text{TOT,SNT}}$). Figure 15 shows the IE t_{TOT} distribution over its start time in the cycle. As in the case of amplitude distributions, the regions with dominating noise (short t_{TOT}), γ (intermediate t_{TOT}) and neutron (longer t_{TOT}) events can be observed. Event t_{TOT} is observed to be rather strongly correlated with the amplitude as indicated in Fig. 16. Hence, only one parameter, either S_{NDT} or $t_{\text{TOT,SNT}}$, is sufficient for single neutron identification. Due to finer granularity and larger range, amplitude is considered to be a better choice and is planned to be used for online nBLM data processing.

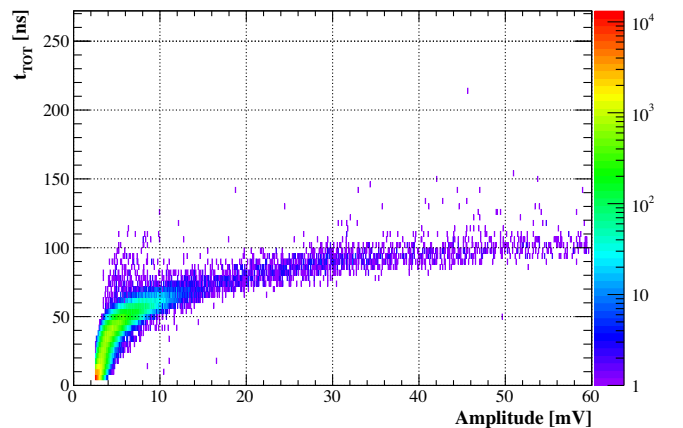


FIG. 16. Correlation between IE amplitude and t_{TOT} for the data collected during the controlled loss experiment.

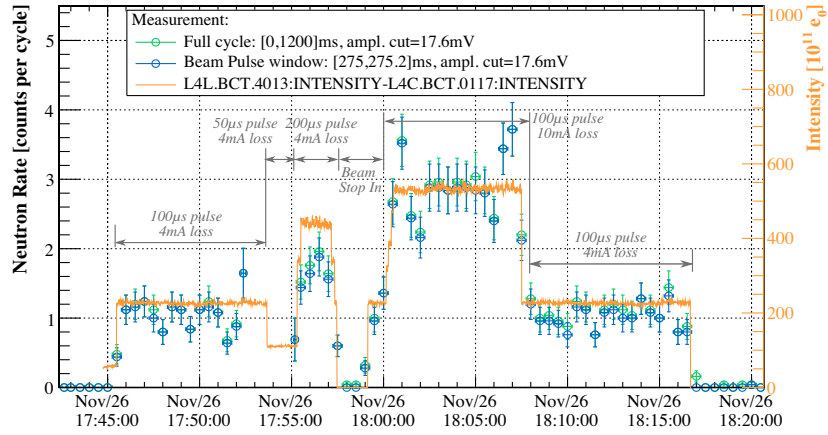


FIG. 17. Estimated neutron rates (green and blue) during controlled loss experiment together with the differential BCT signal (orange). See text for details.

Estimated neutron rates during the controlled loss experiment are presented in Fig. 17. The rate was extracted from EventInfo data through offline analysis by applying the above-mentioned value S_{NDT} as the threshold cut on amplitude for neutron identification. It represents the average number of neutrons per machine cycle observed in maximum beam pulse window (blue) or full machine cycle (green). The averaging was performed over 30 s. The difference in signal from the two previously mentioned BCTs is shown in Fig. 17 as well (orange curve) for comparison. The extracted neutron rate is observed to follow the BCT signal differences rather well, with smaller discrepancies attributed to the difference in loss detection coverage between the nBLM and differential BCT measurement. The result is in agreement with the results extracted from the data recorded with oscilloscope [10].

The data was continuously recorded for more than two weeks after the controlled loss experiment. Measured neutron rates during two different time periods are shown in Figs. 18 and 19. Here, the rates were calculated in the same way as in the case of Fig. 17. However, a different

detector voltage configuration was used in this case compared to the controlled loss experiment, namely $V_{\text{mesh/drift}} = 525/1475$ V instead of $V_{\text{mesh/drift}} = 550/1500$ V. Thus, a different value for S_{NDT} was applied in the offline analysis. The value was extracted as described for controlled loss experiment and was found to be $S_{\text{NDT}} = 9.4$ mV.

Observed neutron rates during LINAC4 commissioning activities focused on sections further downstream of the nBLM detector were typically found to be on the order of 10^{-1} counts/s as seen in Fig. 18. The results in Fig. 19 refer to a day where the commissioning activities were focused on the DTL tank 1 cavity phase and amplitude scans. For comparison, the DTL tank 1 phase recorded by LINAC4 commissioning team during this day is also shown on the bottom plot in Fig. 19 (red curve). For most of the top plot in Fig. 19 the measured rates (blue or green) follow the difference between the two BCT signals (orange curve) rather well, though some differences are to be expected due to the considerable distance between the BCTs and the nBLM detector. However, larger discrepancies in the initial part can be observed in three different time windows, where

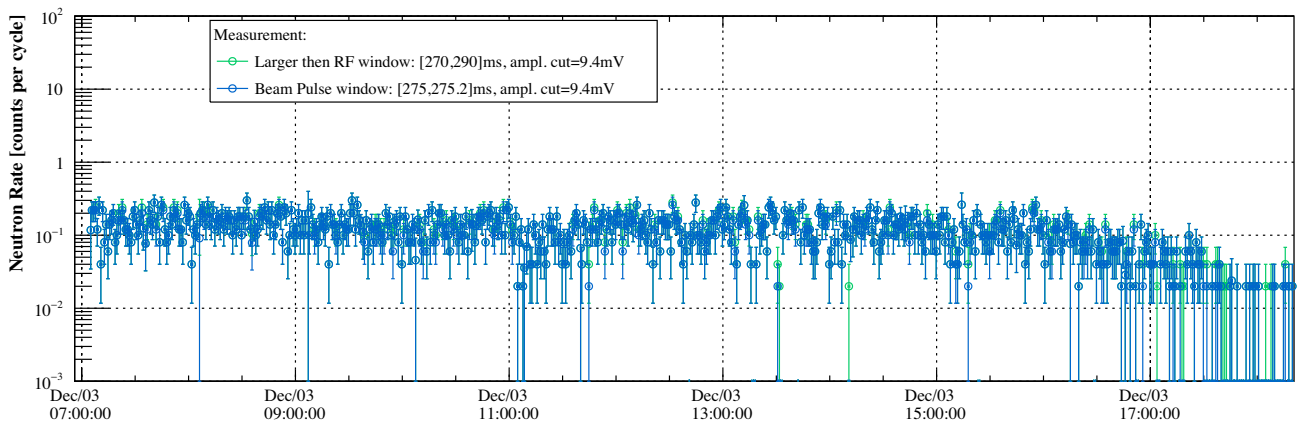


FIG. 18. Example of estimated neutron rates during a typical day with LINAC4 commissioning activities focused on sections further downstream of the nBLM detector.

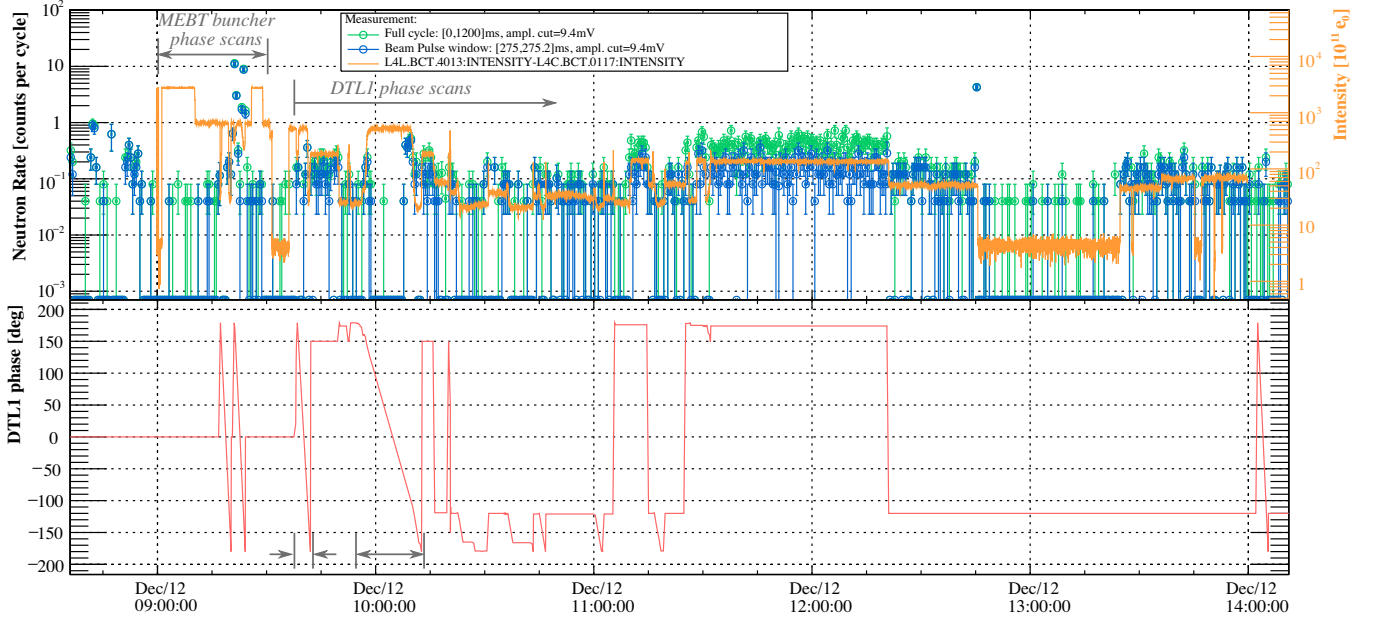


FIG. 19. Example of estimated neutron rates (top) during LINAC4 commissioning activities focused on phase scans of cavities upstream of the nBLM detector. See text for details.

increased loss levels were estimated from differential BCT signal, while a noticeable drop can be observed in the extracted nBLM neutron rates. The behavior can be qualitatively explained by taking into account the LINAC4 commissioning activities performed during this time. In the time window between 9:00 and 9:30 phase scans with MEBT bunchers were performed, hence, the 3 MeV beam was likely lost before reaching the DTL tank 1 and the nBLM detector at the end of the tank. After around 9:30 the focus of commissioning activities moved to DTL tank 1 phase scans. A second period with noticeable discrepancy between nBLM and BCT curves can be observed around 9:40 followed by a third one at around 10:00 (marked with grey arrows on the bottom plot in Fig. 19). These two periods match with the DTL tank 1 phase scan over larger range (from -180 deg to 180 deg). Thus, the discrepancies may be explained by deceleration of the beam. The beam may have been lost at the initial parts of the DTL tank 1. Moreover, if the losses did reach the nBLM detector, the energy of lost beam particles may have been too low for a significant neutron production rate resulting in decreased neutron rates measured with the nBLM detector (see [29] for neutron production cross section on copper).

The remaining two NDA parameters, average single neutron charge ($\langle Q_{TOT} \rangle$) and TOT time limit for identifying pileup events ($t_{TOT,PUT}$), are not discussed here. They require both PU and SN events present in order to find the values that assure smoothest online transition between SNC and Q-method. These parameters are planned to be explored through a simulation using the data collected at LINAC4 to generate the PU events. Experimental

verification is foreseen to be performed at IPHI (High-Intensity Proton Injector) proton beam at CEA Saclay, where neutron fields with rates leading to PU events can be produced by transporting the proton beam on a beryllium target.

VIII. SUMMARY AND OUTLOOK

A neutron sensitive BLM system has been developed for the ESS linac. It is based on Micromegas detectors specially designed for the low-energy part of the ESS linac. Through real-time FPGA-based data processing, the system offers the ability to discriminate beam loss-induced fast neutrons from both the rf-induced photons and background slow neutrons on an event-by-event basis. Part of the system is planned to be installed in the first sections of the ESS linac (MEBT and DTL tank 1) and commissioned toward the end of 2021 and in early 2022.

Two test campaigns have been carried out under realistic conditions at LINAC4 at CERN with a prototype comprising an nBLM-F detector. The results were found to be in accordance with the oscilloscope data [9,10] collected in parallel or separately.

Partially processed data collected at LINAC4 were used to propose a procedure for configuring the values of parameters for neutron detection algorithm. The findings are presented in this paper and are focused on the parameters crucial for single neutron detection. The discussed results are expected to be applicable to both nBLM-F and nBLM-S, as the two detector types exhibit equivalent signal time characteristic. The remaining parameters that were not discussed here are related to neutron pileup event

identification. They are planned to be first investigated through simulation exploiting the single neutron data recorded at LINAC4, while experimental verification is foreseen to take place at IPHI at CEA Saclay.

ACKNOWLEDGMENTS

The authors wish to thank Christos Zamantzas, Jiří Král and William Viganò for their valuable help with detector installation and realization of the test at LINAC4. The authors would also like to gratefully acknowledge the help of Bettina Mikulec and the LINAC4 operation team for making the controlled loss experiment at LINAC4 possible as well as valuable information and help with interpretation of the results. Additionally, the authors thank to Cecilia Maiano for helpful discussions on rf cavity theory and γ background. L. Segui would furthermore like to acknowledge the financial support of Enhanced Eurotalents program (an FP7 Marie Skłodowska-Curie COFUND program).

-
- [1] S. Peggs *et al.*, ESS technical design report, Technical Report No. ESS-DOC-274, ESS ERIC, Lund, Sweden, 2013, <http://eval.ess.lu.se/cgi-bin/public/DocDB/ShowDocument?docid=274>.
 - [2] R. Garoby *et al.*, The european spallation source design, *Phys. Scr.* **93**, 014001 (2018).
 - [3] I. D. Kittelmann *et al.*, Ionisation chamber based beam loss monitoring system for the ESS linac, in Proc. 8th International Beam Instrumentation Conference (IBIC'19), Malmö, Sweden, 8–12 September 2019, International Beam Instrumentation Conference No. 8 (JACoW Publishing, Geneva, Switzerland, 2019), pp. 136–140, [10.18429/JACoW-IBIC2019-MOPPO23](https://doi.org/10.18429/JACoW-IBIC2019-MOPPO23).
 - [4] Y. Giomataris, Development and prospects of the new gaseous detector “Micromegas”, *Nucl. Instrum. Methods Phys. Res., Sect. A* **419**, 239 (1998).
 - [5] I. D. Kittelmann and T. Shea, Simulations and detector technologies for the beam loss monitoring system at the ESS linac, in Proc. of ICFA Advanced Beam Dynamics Workshop on High-Intensity and High-Brightness Hadron Beams (HB'16), Malmö, Sweden, 3–8 July 2016, ICFA Advanced Beam Dynamics Workshop on High-Intensity and High-Brightness Hadron Beams No. 57 (JACoW, Geneva, Switzerland, 2016), pp. 553–558, [10.18429/JACoW-HB2016-THAM6Y01](https://doi.org/10.18429/JACoW-HB2016-THAM6Y01).
 - [6] I. D. Kittelmann, Monte Carlo simulations of beam loss in the DTL, Technical Report No. ESS-0066428, ESS ERIC, Lund, Sweden, 2016.
 - [7] L. Segui, Monte Carlo results: nBLM response to ESS scenarios, Technical Report No. ESS-0513010, ESS ERIC, Lund, Sweden, 2017.
 - [8] J. Norem, A. Moretti, and M. Popovic, The radiation environment in and near high gradient rf cavities, *Nucl. Instrum. Methods Phys. Res., Sect. A* **472**, 600 (2001).
 - [9] L. Segui *et al.*, Characterization and first beam loss detection with one ESS-nBLM system detector, in Proc. 8th International Beam Instrumentation Conference (IBIC'19), Malmö, Sweden, 8–12 September 2019 Shanghai, International Beam Instrumentation Conference No. 8 (JACoW Publishing, Geneva, Switzerland, 2019), pp. 28–34, [10.18429/JACoW-IBIC2019-MOBO04](https://doi.org/10.18429/JACoW-IBIC2019-MOBO04).
 - [10] L. Segui *et al.*, Detector design and performance tests of the ESS-neutron Beam Loss Monitor detectors (2022).
 - [11] T. Papaevangelou *et al.*, ESS nBLM: Beam loss monitors based on fast neutron detection, in Proc. 61st ICFA Advanced Beam Dynamics Workshop (HB'18), Daejeon, Korea, 17–22 June 2018, ICFA Advanced Beam Dynamics Workshop No. 61 (JACoW Publishing, Geneva, Switzerland, 2018), pp. 404–409, [10.18429/JACoW-HB2018-THA1WE04](https://doi.org/10.18429/JACoW-HB2018-THA1WE04).
 - [12] L. Segui *et al.*, A micromegas based neutron detector for the ESS beam loss monitoring, in Proc. 7th International Beam Instrumentation Conference (IBIC'18), Shanghai, China, 9–13 September 2018, International Beam Instrumentation Conference No. 7 (JACoW Publishing, Geneva, Switzerland, 2019), pp. 211–214, [10.18429/JACoW-IBIC2018-TUPA02](https://doi.org/10.18429/JACoW-IBIC2018-TUPA02).
 - [13] S. Agostinelli *et al.*, GEANT4 - a simulation toolkit, *Nucl. Instrum. Methods Phys. Res., Sect. A* **506**, 250 (2003).
 - [14] J. Allison *et al.*, Geant4 developments and applications, *IEEE Trans. Nucl. Sci.* **53**, 270 (2006).
 - [15] J. Allison *et al.*, Recent developments in Geant4, *Nucl. Instrum. Methods Phys. Res., Sect. A* **835**, 186 (2016).
 - [16] T. Kittelmann *et al.*, Geant4 based simulations for novel neutron detector development, *J. Phys.: Conf. Ser.* **513**, 022017 (2014).
 - [17] K. Kanaki, T. Kittelmann, X. X. Cai, E. Klinkby, E. B. Knudsen, P. Willendrup, and R. Hall-Wilton, Simulation tools for detector and instrument design, *Physica B: Condensed Matter* **551**, 386 (2018).
 - [18] IOxOS Technologies SA, ADC3111 (<https://www.ioxos.ch/produit/adc-3110-3111/>).
 - [19] IOxOS Technologies SA, IFC1410 (https://www.ioxos.ch/produit/ifc_1410/).
 - [20] M. Carroll *et al.*, Beam Interlock System concept of operation, Tech. Rep. ESS-0275481 (ESS ERIC, Lund, Sweden, 2021).
 - [21] J. J. Jmroz *et al.*, Timing system integration with MTCA at ESS, in Proc. 17th International Conference on Accelerator and Large Experimental Physics Control Systems (ICALEPCS'19), New York, NY, USA, International Conference on Accelerator and Large Experimental Physics Control Systems No. 17 (JACoW Publishing, Geneva, Switzerland, 2020), pp. 1264–1268, [10.18429/JACoW-ICALEPCS2019-WEPHA071](https://doi.org/10.18429/JACoW-ICALEPCS2019-WEPHA071).
 - [22] EPICS—Experimental Physics and Industrial Control System (<https://epics-controls.org/>).
 - [23] CAEN SpA, SY4527 (<https://www.caen.it/products/sy4527/>).
 - [24] CAEN SpA, A7030 (<https://www.caen.it/products/a7030/>).
 - [25] CAEN SpA, A2519 (<https://www.caen.it/products/a2519/>).
 - [26] G. Jabłoński, I. D. Kittelmann, W. Jałmużna, R. Kiełbik, W. Cichalewski, K. Rosengren, T. Shea, F. d. Santos Alves, V. Grishin, T. Papaevangelou, L. Segui, and C. Zamantzas, FPGA-based data processing in the neutron-sensitive beam loss monitoring system for the ESS linac, in 2019 MIXDES—26th International Conference “Mixed Design of Integrated Circuits and Systems”, Rzeszów, Poland, 27–19 June 2019

- (IEEE, New York, 2019), pp. 101–105, [10.23919/MIXDES.2019.8787166](#).
- [27] A. Lombardi, Commissioning of CERN LINAC4, in Proc. 29th Linear Accelerator Conference (LINAC'18), Beijing, China, 16–21 September 2018, Linear Accelerator Conference No. 29 (JACoW Publishing, Geneva, Switzerland, 2019), pp. 658–662, [10.18429/JACoW-LINAC2018-TH1P01](#).
- [28] M. Vretenar *et al.*, Linac4 design report, CERN Yellow Reports: Monographs Vol. **6** (CERN, Geneva, Switzerland, 2020), [10.23731/CYRM-2020-006](#).
- [29] R. Collé, R. Kishore, and J. B. Cumming, Excitation functions for (p, n) reactions to 25 MeV on ^{63}Cu , ^{65}Cu , and ^{107}Ag , *Phys. Rev. C* **9**, 1819 (1974).